RSC Advances

# Manganese Dioxide Nanoparticles Incorporated within Ionic Liquid Derived Fibrillated Mesoporous Carbon: Electrode Material for High-Performance Supercapacitors

| | |
|---|---|
| Journal: | *RSC Advances* |
| Manuscript ID | RA-ART-08-2015-016923.R1 |
| Article Type: | Paper |
| Date Submitted by the Author: | 21-Sep-2015 |
| Complete List of Authors: | Kazemi, Sayed Habib; IASBS University, Chemistry<br>Karimi, Babak; IASBS University, Chemistry<br>Fashi, Armin; IASBS University, Chemistry<br>Behzadnia, Hesam; IASBS University, Chemistry<br>Vali, Hojatollah; McGill University , , H3A 2A7 Canada, Anatomy and Cell Biology and Facility for Electron Microscopy Research |
| Subject area & keyword: | |
| | |

# Manganese Dioxide Nanoparticles Incorporated within Ionic Liquid Derived Fibrillated Mesoporous Carbon: Electrode Material for High-Performance Supercapacitors

*Sayed Habib Kazemi*[*,a,b]*, Babak Karimi*[*,a]*, Armin Fashi* [a]*, Hesam Behzadnia* [a]*,*
*Hojatollah Vali* [c]

[a] *Department of Chemistry, Institute for Advanced Studies in Basic Sciences (IASBS) Zanjan 45137-66731 (Iran)*

[b] *Center for Research in Climate Change and Global Warming (CRCC), Institute for Advanced Studies in Basic Sciences (IASBS), Zanjan 45137-66731, Iran*

[c] *Department of Anatomy and Cell Biology and Facility for Electron Microscopy Research, McGill University, 3450 University St. Montreal, Quebec, H3A 0C7 (Canada)*

*E-mail addresses: habibkazemi@iasbs.ac.ir, karimi@iasbs.ac.ir Fax: +98-241-4153232*

## Abstract:

Present article is the first example of incorporation of metal oxide nanoparticles within the ionic liquid derived nano-fibrillated mesoporous carbon (IFMC); as the electrode materials for supercapacitor applications. Electron microscopy observations, X-ray diffraction analysis, in addition to gas adsorption/desorption analysis confirm the incorporation of manganese dioxide within the mesoporous nanofibers ($MnO_2$@IFMC) with high surface area of about 388 $m^2$ $g^{-1}$. $MnO_2$@IFMC was successfully employed as new electrode material for high-rate supercapacitors in neutral media. The one-dimensional nano-composite shows high performance and excellent cycle life stability according to electrochemical studies. This substantial performance and high specific capacitance may be originated from the high surface area of nano-composite, shortened diffusion length and mesoporous openings on the outer surface. Also, augmented conductance of the carbon nanofibers due to heteroatom (nitrogen) effect can be considered as important reason for high-rate capability and excellent specific capacitance (almost 1000 F $g^{-1}$ at 10 mV $s^{-1}$). Our results indicate that $MnO_2$@IFMC can be considered as promising electrode material for high-rate supercapacitors.

Keywords: Mesoporous carbon; Supercapacitor; Specific Capacitance; Nanostructures; Conducting materials.

## 1. Introduction

Porous carbon materials, especially mesoporous carbons have attracted a great intense of researches due to their unique properties including excellent chemical stability, high available surface area, and easily accessed pore channels [1-4]. Carbon materials containing heteroatoms were found to exhibit improved physical and chemical properties. In addition to the high real surface area, these nanostructures provide a shortened path length for the electron transport. The greatly enhanced electrolyte penetration and shortened diffusion length for electrons and the ions are of high importance for the high capacitance and high-rate capable supercapacitors [2, 5]. Electrochemical supercapacitors have been attracted an enormous profound of researches as important energy storage systems because of their ability to deliver high power and preserving the stable operation, especially stability in their specific capacitance, during thousands of charge-discharge cycles [2, 5-9]. Considering the various mechanisms of charge storage in the supercapacitor systems, there are two types of such energy storage systems: Electrical double layer capacitors (EDLCs) and electrochemical pseudocapacitors. The mechanism for the first type systems is based on the electrostatic forces while the second type works through fast Faradaic redox reactions [6, 10-13]. Recently, conducting polymers, also electroactive metal oxides and hydroxides have been frequently investigated as electroactive materials in electrochemical supercapacitor systems, because of affording high theoretical specific capacitance arising from redox reactions [14-21]. A wide variety of transition metal oxides and hydroxide nanostructures are of important candidates as electrode materials to design the supercapacitor electrodes[10, 14, 15, 18, 22-28]. Among them, manganese oxides and hydroxides are of particular importance because of their low price, high theoretical specific capacitance and low toxicity [29]. It should be mentioned that the carbon nanostructures can afford the platform for decorating the metal oxide nanostructures to circumvent their agglomeration, thus providing superior utilization of such materials [2, 11, 30, 31].

For carbon based materials incorporated with transition metal oxides, the charge storage mechanisms relies on both electrical double-layer mechanisms in addition to the contribution of the redox reactions [7, 10, 13, 23, 32-42]. Thus, it could be possible to overcome the low specific capacitance of carbon materials. Of course, another important shortcoming of commercial supercapacitors is the low energy density. To date, this problem have implemented substantial challenges towards the application of commercial supercapacitors as primary power sources instead of batteries [32]. It is concluded that dispersing the $MnO_2$ nanoparticles on conductive substrates could result in accomplishing the redox reactions in charge storage mechanism by enhancing the electrical conductivity of the $MnO_2$ based electrodes [34]. Of course, increasing the electrical conductivity and specific capacitance will be possible if forming a high surface-area metal oxide layer while preserving high conductivity of the electrode even at a high oxide loading [34].

Two important shortcomings of commercial supercapacitor materials are the limited specific capacitance of carbon materials in addition to low energy density [34, 43-45]. Charge storage mechanisms in transition metal oxides incorporated carbon materials include both the based on both electrical double-layer mechanisms in addition to the contribution of the redox reactions [32, 46]. Thus, it could be possible to enhance the low specific capacitance of carbon materials by incorporation of metal oxides nanostructures [14]. Thus, involvement of nanoparticles of metal oxides and hydroxides in the electrode materials may result in the enhanced energy density; also increasing the operational potential windows of the supercapacitors by forming a high real surface area of metal oxide layer while maintaining adequate conductivity of the electrode even at a high metal oxide loading [7, 12, 14, 23].

Recently, we have synthesized and reported the catalytic, electrochemical and supercapacitive behaviors of novel ionic liquid derived mesoporous carbons (IFMC and IOMC) in which a high specific capacitance and high rate capability was observed, as well as interesting electrochemical behaviors [45, 47, 48]. Herein, we investigate the incorporation of $MnO_2$ nanoparticles within IFMC and its supercapacitive behavior. Our results corroborate the high specific capacitance and energy density for IFMC-$MnO_2$ electrode, indicating excellent and tunable conductivity of carbon substrate as well as the large real surface area of IFMC-$MnO_2$ nanocomposite.

## 2. Experimental and methods

### *2.1. Preparation of $MnO_2$@IFMC*

All chemicals were purchased from Sigma-Aldrich and Alfa Aesar companies and used as received. Synthesis of the ionic liquid derived nano-fibrillated mesoporous carbon (IFMC) was achieved based on the previously reported work by Karimi et al [1]. To synthesize IFMC, a dry acetonitrile solution of IL (1-methyl-3-phenethyl-1H-imidazolium hydrogen sulfate) was added drop-wise to a suspension of SBA-15 in acetonitrile. After 24 h of stirring at room temperature, the solvent was removed under reduced pressure. The resultant powder was impregnated with an aqueous solution of sulfuric acid and placed in a vacuum drying oven until a dark brown powder was obtained. This composite was then kept in an argon flow at 900 °C for 3 h to carbonize the IL. To remove the silica template, the black powder was stirred in a solution of sodium hydroxide at 50 °C for 24 h. The filtered nanoporous carbon was washed several times with deionized water and ethanol and vacuum dried. To prepare $MnO_2$@IFMC nanocomposite, a solution of urea was slowly added to an aqueous suspension of IFMC and manganese acetate. During the addition of urea IFMC containing suspension was stirred and sonicated, also its temperature fixed at 40 °C. Then, to purify the $MnO_2$@IFMC product, centrifugation and washing with distilled water was carried out. The resulting precipitation which appeared as a black powder was left in an oven at 80 °C to dry. Finally, thermal treatment of the $MnO_2$@IFMC product was performed at 280 °C in and electrical oven for 3 hours.

### *2.2. Electrochemical investigations*

To prepare the supercapacitor electrodes, a mixture of $MnO_2$@IFMC powders, poly-tetraflouro ethylene (PTFE) and acetylene black powder in a ratio of 80:10:10 was loaded onto the carbon paper electrode as current collector and left to dry under vacuum at 100 $^{o}$C for at least 4 hours. Electrochemical measurements were carried out in both three and two electrodes systems. A Zahner-Zennium Potentiostat-Galvanostat instrument in addition to Autolab 101 (Eco Chemie Bv Netherlands) was employed for electrochemical studies. Ac impedance spectroscopy measurements were carried out in the frequency range of 100 kHz to 10 mHz by applying a 5 mV amplitude ac voltage. Also, EIS results were analyzed by using the complex nonlinear least square (CNLS) fitting method. Two electrode measurements were performed on a symmetrical combination of two identical $MnO_2$@IFMC electrodes in which the electrodes were separated by a thin separator. It should be noted that a solution of 1 M $Na_2SO_4$ was injected as electrolyte.

### *2.3. Characterization*

The morphology and structure of the samples were examined by field emission scanning electron microscopy (FESEM, Hitachi S-4160, equipped with energy dispersive X-ray analyzer (EDAX)), transmission electron microscopy (TEM, Hitachi-600, Japan), and $N_2$ adsorption-desorption measurements by using a Belsorp instrument (BELMAX, Japan). XRD analysis was carried out by using a D8 XRD Advance Bruker instrument. Thermal analysis (TG-DSC) was performed by a NETZSCH STA 409 PC/PG.

## 3. Results and discussion

### *3.1. Surface characterization of* $MnO_2$@IFMC

### *3.1.1. Electron microscopy and EDAX analysis*

Figure 1A shows a typical SEM top-view image of the $MnO_2$@IFMC nanocomposite. From these Figures, the $MnO_2$ nanoparticles can be observed on the outer surface of IFMC. The SEM image of $MnO_2$@IFMC nanocomposite demonstrates that the composite possesses a branched spongy structure. However, to see the mesoporous structure of IFMC, TEM images are necessary. TEM image (Figure 1B) shows the fibrilliar structure of nanocomposite in which homogenous incorporation of $MnO_2$ can be seen. Higher resolution TEM image of $MnO_2$@IFMC nanocompositeis provided as Figure 1C. From TEM images, we can see the nano-fibrillated structure of the IFMC in which approximately 10 nm $MnO_2$ nanoparticles incorporated. To compare the effect of incorporation of metal oxide nanoparticles on IFMC structure, TEM image of pure IFMC is also provided in supporting information (Figure S-1). It is clear that the nano-fibrilliar structure is almost retained after composite formation providing high active surface area in electrochemical studies. This finding is in good agreement with the porosimetry results. Also, EDAX analysis confirmed the presence of manganese in the structure of $MnO_2$@IFMC nanocomposite (Figure 2). Moreover, Figure S-2 supports the presence of nitrogen heteroatom in IFMC substrate by X-ray photoelectron spectroscopy (XPS).

**Figure 1 and Figure 2**

### *3.1.2. XRD analysis*

Figure 3 gives the XRD patterns of $MnO_2$@IFMC. The pattern of $MnO_2$@IFMC can be compared with the patterns of α-$MnO_2$ [24, 32]. The peaks appeared approximately at 30°, 37°, 60°, 66° and 69° correspond to (310), (211), (521), (002) and (541) crystal planes which are in good agreement with α-$MnO_2$ (JCPDS no. 44-0141). Although, the main phase can be attributed to α-$MnO_2$, a few other phases, such as γ-$MnO_2$ may also be present. The relatively intensive and sharp peak appeared at almost 32° is attributed to the graphitic structure of IFMC carbon. The diffraction peaks of $MnO_2$ were found to be relatively broadened and of lower intensity as compared to the carbon fiber peaks. This implies low degree of crystallinity and the small grain size of the manganese oxide nanostructure. The average size of the manganese oxide nanoparticles incorporated into IFMC was approximately estimated as 10 nm using Scherrer's equation:

$$D = \frac{0.9\lambda}{W cos\theta} \qquad \text{eq (1)}$$

where λ is the X-ray wavelength, W is the full width at half-maximum (FWHM), and θ is the Bragg angle. The average size of $MnO_2$ nanoparticles is in good agreement by TEM measurements.

**Figure 3**

### *3.1.3. Porosimetry*

The nitrogen adsorption–desorption isotherms were recorded to investigate the effect of loading and incorporating of $MnO_2$ nanostructures on IFMC characteristics. The $N_2$ isotherm of IFMC-$MnO_2$ is of classical type IV with a clear hysteresis loop at pressures of 0.2−0.9 (Figure 4A), indicating the presence of mesopores in the $MnO_2$@IFMC product as confirmed by TEM images. Also, Figure 4B represents the distribution of the pore size of the synthesized $MnO_2$@IFMC materials. The BET specific surface area, measured from the nitrogen adsorption isotherm, was found to be 388 $m^2g^{-1}$.The pore diameters was calculated by the BJH method. The maximum pore diameter distribution was less than 5 nm (Figure 4B). The $N_2$-sorption diagram also indicates the coexistence of micropores and mesopores. The specific surface area was decreased after impregnation of $MnO_2$ nanoparticles from 778$m^2$ $g^{-1}$ to 388 $m^2$ $g^{-1}$ possibly due to blocking of some of the mesopores and channels. However, $MnO_2$@IFMC still preserved a high surface area which is quite suitable for supercapacitor purposes. It should be noted that the pore volume was decreased from 0.98 $cm^3$ $g^{-1}$ to 0.39 $cm^3$ $g^{-1}$for pure IFMC and $MnO_2$@IFMC, respectively. The decrease in pore volumes might be originated from the formation of metal oxide within nanospaces of pristine IFMC. The nature of the $N_2$ adsorption–desorption isotherm demonstrates insignificant changes upon impregnation of $MnO_2$, indicating that the mesoporous structure was mostly retained after incorporation of $MnO_2$. This finding is reasonably in agreement with TEM observations of pure IFMC and $MnO_2$@IFMC. The mesoporous structure of IFMC with interconnections (secondary mesoporous structure) can provide a constructive path for electrolyte ion transportation and penetration. This behavior could result in the fast ion transfer and consequently faster charge-discharge ability of the electrode materials for supercapacitor applications.

**Figure 4**

### *3.1.3. Thermal analysis*

TGA was used to examine the loading of $MnO_2$ and thermal decomposition of the as-prepared nanocomposite under air at a heating rate of 10 °Cmin$^{-1}$. The curves of weight loss and derivative weight change of $MnO_2$@IFMC are shown in Figure 5. As the temperature was increased to 100 °C, the sample weight decreased slightly due to desorption of water content. Also, $MnO_2$@IFMC nanocomposite is stable until 300 °C and the weight loss between 100 to 330 °C is almost 2 %. The major weight loss occurred within the range of 300-400 °C (the sharp peak of weight loss is located at almost 330 °C) can be attributed to the combustion of carbon content in the samples. As shown on TGA plots, the graphitic carbon content of the nanocomposite,which is lost at almost 330 °C, can be estimated as almost 41 %. The residual weight observed after 450 °C can be taken into account for $MnO_2$ nanoparticles weight. The residual mass of the sample was almost 42 % which shows high loading of $MnO_2$ nanoparticles into IFMC structure.

**Figure 5**

### *3.2. Voltammetric behavior of IFMC-based electrode*

Figure 6 illustrates the cyclic voltammograms recorded for $MnO_2$@IFMC based electrode in a 1.0 M $Na_2SO_4$ solution. As it can be clearly seen, the shape of the voltammograms is almost rectangular; indicating the nearly ideal supercapacitive behavior of the employing electrode material. Figure 7 displays the specific capacitances of $MnO_2$@IFMC electrode against the scan rates; which estimated as 1100, 978, 890, 844, 800 and 744 F g$^{-1}$ at scan rates of 10, 20, 50, 100, 200 and 400 mV $s^{-1}$, respectively. These excellent specific capacitances are mainly originated from the monotonous distribution of $MnO_2$ nanoparticles within IFMC structure, in addition to large surface area and good conductivity provided by IFMC substrate. Notably, $\alpha$-$MnO_2$ was revealed to be the major metal oxide phase according to XRD analysis. This is an important observation because it may indeed result in facile electron/ion insertion reaction, especially hydrated cations. Of course, considerable high surface area can be expected for $MnO_2$ nanoparticles due to high surface area of IFMC substrate. Such a high effective surface for $MnO_2$ nanostructures seems to play an essential role to produce high specific capacitance in IFMC-$MnO_2$ nanocomposite. It was reported that the transportation of alkali cations (usually $Li^+$, $Na^+$ and $K^+$) into the bulk of $MnO_2$ nanostructures is responsible for the main part of electrical charge capacitance [49].

$$\mathrm{MnO_2} + M^+ + \mathrm{e}^- \rightleftharpoons \mathrm{MnOO}M$$

$$(M^+ = \mathrm{Li}^+, \mathrm{Na}^+, \mathrm{K}^+)$$

It was observed that the specific capacitance decreased by increasing the scan rate, due to the commonly proposed mechanism for charge storage process in $MnO_2$ nanostructures. At low scan rates, almost all of the pores within the structure are accessible for electrolyte ions; results in complete ion movement into and out of the pores. While at higher scan rates, the effective diffusion of ions into the electrode structure is reduced and only the outer surface and top surface of larger pores involved in ion insertion/extraction; leading to reduced specific capacitance [39-42, 50]. In the present work, for $MnO_2$@IFMC nanocomposite electrode, the diffusion of $Na^+$ ions into the $MnO_2$ nanostructures was slightly decreased at higher scan rates, although the major part of capacitance is most likely originated from charging of outer surface of the electrode material. It may be concluded that only a small fraction of interior surface of $MnO_2$ nanoparticles and deep pores of the IFMC does not actively contribute to the capacitance at higher scan rates. The superior structure of IFMC material is very essential to reach the ions to the much of the deeper active sites, thus it leads to slight decrease in capacitance at high scan rates. Figure 7 represents the estimated specific capacitance against potential scan rate, estimated from voltammograms in Figure 6. As shown in Figure 7, the specific capacitance was decreased about 25% from 10 to 200 mV $s^{-1}$, suggesting the high-rate capability of IFMC-$MnO_2$ nanocomposite.

**Figure 6 and Figure 7**

### *3.3. Galvanostatic charge-discharge experiments of IFMC-based electrode*

Charge-discharge experiments were carried out at different current density to evaluate the specific capacitance of the electrode materials, also to confirm the cyclic voltammetry results. Figure 8a shows a typical plot of galvanostatic charge-discharge curves recorded for $MnO_2$@IFMC nanocomposite-based electrode at a discharge current of 8.88 A $g^{-1}$. The specific capacitance can be estimated using the following equation:

$$C = \frac{i\Delta t}{m\Delta V} \qquad \text{eq(2)}$$

where $C$ (F $g^{-1}$) is the specific capacitance, $i$ (mA) is charge-discharge current, $\Delta t$ (s) is discharge time, $m$ (mg) is the mass of $MnO_2$@IFMC that used in constructing the supercapacitor electrode, and $\Delta V$ (V) represents the potential drop of discharge curve. Also, Figure 8b demonstrates the variations of specific capacitance estimated for $MnO_2$@IFMC electrode against current density. As can be seen in Figure 8b, a slight decrease in specific capacitance with increasing the current density has been occurred. The slight decrease in capacitance may be attributed to possible charge storage in the interior of $MnO_2$@IFMC electrode surface, as well as outer spaces, even at high discharge rates (current densities). It should be noted that almost 80% of specific capacitance at a current density of 4.4 A $g^{-1}$ was preserved at 17.7 A $g^{-1}$, suggesting the exceptional high-rate performance of electrode material.

Figure 9 displays the Ragone plot (power density vs. energy density) for $MnO_2$@IFMC electrode. According to this plot, maximum power and energy density of 4.63 kW $kg^{-1}$ and 25.3 Wh $kg^{-1}$, can be acquired of $MnO_2$@IFMC electrode. The values obtained for energy and power densities are interestingly comparable to the previously reported works based on the metal oxide nanostructures used for supercapacitor purposes; even the specific energy density obtained for $MnO_2$@IFMC is improved [14, 20]. Additionally, energy density was decreased slightly with increasing the power density, signifying the high performance behavior of IFMC-$MnO_2$ electrode material.

**Figure 8 and Figure 9**

### *3.4. Electrochemical impedance analysis of IFMC-based electrode*

Figure 10 illustrates the Nyquist plot of $MnO_2$@IFMC nanocomposite-based electrodes recorded at the open circuit potential. In the high and middle frequency region a very small charge transfer resistance was observed; indicating the low charge transfer resistance for $MnO_2$@IFMC nanocomposite-based electrodes. Also, the depressed semicircle is ended by a vertical line in the low frequency region. To find the electrical parameters for the supercapacitor electrode, EIS results were well fitted to appropriate equivalent circuit (shown as Scheme 1). The equivalent series resistance for the supercapacitor electrode was estimated to be 2.4 Ω and the charge transfer resistance associated with electrode double layer charging was less than 0.2

Ω. Besides, the electrochemical series resistance (ESR) value for $MnO_2$@IFMC electrodes is reasonably low, indicating that the electrode material has very small resistance with good ion response at high-frequency ranges. The slope of the line in the low frequency region is more than 75°; as expected to see for supercapacitive behavior of the electrode material.

**Figure 10**

**Scheme 1**

### *3.5. Electrochemical behavior of two electrode system*

A symmetric two-electrode supercapacitor was constructed by assembly of two identical $MnO_2$@IFMC electrodes to examine the execution of the electrode materials in a real supercapacitor design. Then, complete electrochemical studies of the symmetric two electrode supercapacitor were performed. According to the galvanostatic charge/discharge experiments (results shown as Table 1), there is a modest decrease in the specific capacitance with increasing the discharge current density. As seen in Table 1, the specific capacitance drop was 10% by increasing the current density up to 17.8 A $g^{-1}$. This small decrease in specific capacitance can be ascribed by the appropriate morphology of $MnO_2$@IFMC nanocomposite, in addition to suitable small size and structure of manganese oxide nanoparticles which provide short pathways for diffusion of electrolyte ions. Furthermore, it is not surprising to speculate that this issue might be also due to the high accessible surface area of nanocomposite, which can in turn afford the great part of its surface area to the electrolyte ions at larger current densities. Also, an exceptional specific capacitance of 521 F $g^{-1}$ at a current density of 8.8 A $g^{-1}$ was achieved for a two-electrode assembly. This value can be considered as 1040 F $g^{-1}$ for a single electrode capacitance which is remarkable compared to the theoretical specific capacitance of $MnO_2$ [29]. To check the synergy effect between IFMC and $MnO_2$ nanoparticles, two different experiments were carried out for IFMC pure and $MnO_2$ pure supercapacitors. It should be mentioned that the specific capacitance of pure IFMC electrode was estimated about 110 F $g^{-1}$ at a current density of 9.0 A $g^{-1}$, while this value for $MnO_2$ nanoparticles fabricated in the absence of IFMC was approximately 200 F $g^{-1}$. These findings reveal that incorporation of metal oxide nanoparticles within IFMC structure results in a remarkable synergic effect in charge storage behavior of $MnO_2$@IFMC nanocomposite.

Finally, the cycle life stability is a crucial factor for practical supercapacitor purposes. Herein, the estimated specific capacitance for $MnO_2$@IFMC electrode supercapacitor showed that the electrode materials maintains more than 90% of its initial capacitance after 2000 successive charge-discharge cycles (shown as Figure S-3). Also, the specific capacitance retention was approximately 80% after 5000 charge-discharge cycles; indicating the excellent stability for the electrode material. Thus, the $MnO_2$@IFMC electrode can be proposed as a prominent candidate for construction of high-rate supercapacitor.

**Table1**.

## 4. Conclusion

In the present work introduce a facile method to fabricate the nanocomposite of $MnO_2$ incorporated into the structure of a nano-fibrillated mesoporous carbon. The electrochemical behavior of $MnO_2$@IFMC electrode was studied and it was found that the nanocomposite comprises remarkable charge storage capacitance in addition to high-rate capability. It was concluded that the supercapacitive behavior may be originated from the ordered mesoporous structure with inner connections and high active surface area; enhancing facile Faradic reactions for metal oxide nanoparticles. It is worth mentioning that $MnO_2$@IFMC based electrodes maintain more than 90% of their initial capacitance after 2000 charge-discharge cycles, while capacitance drop by increasing the discharge current was significantly small. Our results suggest the $MnO_2$@IFMC nanocomposite as an excellent alternative electrode material for high-rate supercapacitor applications.

## Acknowledgements

Financial supports of the work by Institute for Advanced Studies in Basic Sciences are acknowledged.

## References

1. B. Karimi, H. Behzadnia, M. Bostina and H. Vali, *Chem. Eur. J.*, 2012, **18**, 8634-8640.
2. K. Wang, Y. Wang, Y. Wang, E. Hosono and H. Zhou, *J. Phys. Chem. C*, 2009, **113**, 1093-1097.
3. E. Khaled, M. S. Kamel, H. N. A. Hassan, A. A. Haroun, A. M. Youssef and H. Y. Aboul-Enein, *Talanta*, 2012, **97**, 96-102.
4. A. M. Youssef, *RSC Advances*, 2014, **4**, 6811-6820.
5. J. Ni, W. Lu, L. Zhang, B. Yue, X. Shang and Y. Lv, *J. Phys. Chem. C*, 2009, **113**, 54-60.
6. S. H. Kazemi, M. A. Kiani, R. Mohamadi and L. Eskandarian, *Bull. Mater. Sci.*, 2014, **37**, 1001-1006.

7. S. H. Kazemi, A. Asghari and M. A. Kiani, *Electrochim. Acta*, 2014, **138**, 9-14.
8. A. Safavi, S. H. Kazemi and H. Kazemi, *Electrochim. Acta*, 2011, **56**, 9191-9196.
9. S. Habib Kazemi and A. Asghari, *Mater. Lett.*, 2015, **142**, 156-159.
10. H. Chen, J. Xu, X. Xu and Q. Zhang, *Eur. J. Inorg. Chem.*, 2013, **2013**, 1105-1108.
11. A. K. Mishra and S. Ramaprabhu, *J. Phys. Chem. C*, 2011, **115**, 14006-14013.
12. C. Liu, Z. Yu, D. Neff, A. Zhamu and B. Z. Jang, *Nano Lett.*, 2010, **10**, 4863-4868.
13. W. Sun, X. Wang, H. Zhu, X. Sun, F. Shi, G. Li and Z. Sun, *Sens. Actuators, B*, 2013, **178**, 443-449.
14. H. Gao, F. Xiao, C. B. Ching and H. Duan, *ACS Appl. Mater. Interfaces*, 2012, **4**, 2801-2810.
15. J. R. McKone, B. F. Sadtler, C. a. Werlang, N. S. Lewis and H. B. Gray, *ACS Catalysis*, 2013, **3**, 166-169.
16. X.-C. Dong, H. Xu, X.-W. Wang, Y.-X. Huang, M. B. Chan-Park, H. Zhang, L.-H. Wang, W. Huang and P. Chen, *ACS nano*, 2012, **6**, 3206-3213.
17. X. Zhao, L. Zhang, S. Murali, M. D. Stoller, Q. Zhang, Y. Zhu and R. S. Ruoff, *ACS nano*, 2012, **6**, 5404-5412.
18. B. Wang, J. S. Chen, Z. Wang, S. Madhavi and X. W. D. Lou, *Adv. Energy Mater.*, 2012, **2**, 1188-1192.
19. S. H. Kazemi, B. Karimi, S. Abdollahi Aghdam, H. Behzadnia and M. A. Kiani, *RSC Advances*, 2015, DOI: 10.1039/C5RA09136E.

20. L. Li, A.-R. O. Raji, H. Fei, Y. Yang, E. L. G. Samuel and J. M. Tour, *ACS Appl. Mater. Interfaces*, 2013, **5**, 6622-6627.

21. F. Manteghi, S. H. Kazemi, M. Peyvandipour and A. Asghari, *RSC Advances*, 2015, **5**, 76458-76463.

22. S.-g. Hwang, S.-h. Ryu, S.-r. Yun, J. Myoun, K. Man and K.-s. Ryu, *Mater. Chem. Phys.*, 2011, **130**, 507-512.

23. B. P. Bastakoti, H. Oveisi, C.-C. Hu, K. C. W. Wu, N. Suzuki, K. Takai, Y. Kamachi, M. Imura and Y. Yamauchi, *Eur. J. Inorg. Chem.*, 2013, **2013**, 1109-1112.

24. Y. Zhang, G.-y. Li, Y. Lv, L.-z. Wang, A.-q. Zhang, Y.-h. Song and B.-l. Huang, *Int. J. Hydrogen Energy*, 2011, **36**, 11760-11766.

25. J. Gomez and E. E. Kalu, *J. Power Sources*, 2013, **230**, 218-224.

26. C. Mondal, M. Ganguly, P. K. Manna, S. M. Yusuf and T. Pal, *Langmuir*, 2013, **29**, 9179-9187.

27. G. S. Gund, D. P. Dubal, B. H. Patil, S. S. Shinde and C. D. Lokhande, *Electrochim. Acta*, 2013, **92**, 205-215.

28. G. Xiong, K. P. S. S. Hembram, R. G. Reifenberger and T. S. Fisher, *J. Power Sources*, 2013, **227**, 254-259.

29. M. Toupin, T. Brousse and D. Bélanger, *Chem. Mater.*, 2004, **16**, 3184-3190.

30. H. Jiang, J. Ma and C. Li, *Adv. Mater.*, 2012, **24**, 4197-4202.

31. D. Saha, Y. Li, Z. Bi, J. Chen, J. K. Keum, D. K. Hensley, H. A. Grappe, H. M. Meyer, S. Dai, M. P. Paranthaman and A. K. Naskar, *Langmuir*, 2014, **30**, 900-910.

32. S. H. Kazemi, M. G. Maghami and M. A. Kiani, *Mater. Res. Bull.*, 2014, **60**, 137-142.

33. X. Zhang, D. Zhao, Y. Zhao, P. Tang, Y. Shen, C. Xu, H. Li and Y. Xiao, *J. Mater. Chem. A*, 2013, **1**, 3706-3706.

34. M. Zhi, A. Manivannan, F. Meng and N. Wu, *J. Power Sources*, 2012, **208**, 345-353.

35. Y. Wang, H. Zhong, L. Hu, N. Yan, H. Hu and Q. Chen, *J. Mater. Chem. A*, 2013, **1**, 2621-2621.

36. J. Ma, Q. Cheng, V. Pavlinek, P. Saha and C. Li, *New J. Chem.*, 2013, **37**, 722-722.

37. R. I. Jafri, A. K. Mishra and S. Ramaprabhu, *J. Mater. Chem.*, 2011, **21**, 17601-17601.

38. Z. Sun and X. Lu, *Ind. Eng. Chem. Res.*, 2012, **51**, 9973-9979.

39. S. C. Pang, M. A. Anderson and T. W. Chapman, *J. Electrochem. Soc.*, 2000, **147**, 444-450.

40. R. K. Sharma, H.-S. Oh, Y.-G. Shul and H. Kim, *J. Power Sources*, 2007, **173**, 1024-1028.

41. G.-R. Li, Z.-P. Feng, Y.-N. Ou, D. Wu, R. Fu and Y.-X. Tong, *Langmuir*, 2010, **26**, 2209-2213.

42. G. Yu, L. Hu, M. Vosgueritchian, H. Wang, X. Xie, J. R. McDonough, X. Cui, Y. Cui and Z. Bao, *Nano Lett.*, 2011, **11**, 2905-2911.

43. J.-G. Wang, Y. Yang, Z.-H. Huang and F. Kang, *J. Power Sources*, 2013, **224**, 86-92.

44. W. Wei, X. Cui, W. Chen and D. G. Ivey, *J. Power Sources*, 2009, **186**, 543-550.

45. S. H. Kazemi, B. Karimi, A. Fashi, H. Behzadnia and H. Vali, *J. Solid State Electrochem.*, 2014, **18**, 2419-2424.

46. H. Sayahi, M. A. Kiani and S. H. Kazemi, *J. Solid State Electrochem.*, 2014, **18**, 535-543.
47. B. Karimi, H. Behzadnia and H. Vali, *ChemCatChem*, 2014, **6**, 745-748.
48. B. Karimi, H. Behzadnia, M. Rafiee and H. Vali, *Chem. Commun.*, 2012, **48**, 2776-2778.
49. S. Pang, M. A. Anderson and T. W. Chapman, *J. Electrochem. Soc.*, 2000, **147**, 444-450.
50. J.-G. Wang, Y. Yang, Z.-H. Huang and F. Kang, *Mater. Chem. Phys.*, 2013, **140**, 643-650.

**Scheme 1.** Equivalent circuit used to fit the experimental EIS data for IFMC-$MnO_2$ nanocomposite

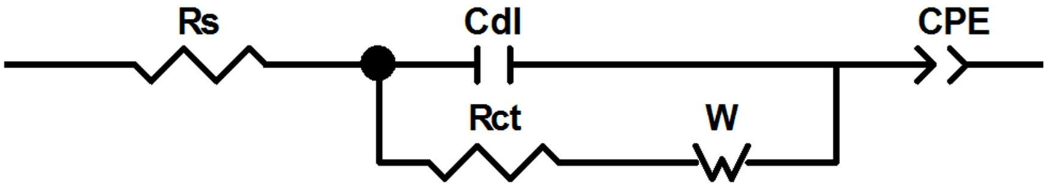

**List of Tables**

**Table1**. Specific capacitances estimated at different current densities for symmetric $MnO_2$@IFMC nanocomposite supercapacitor

| **i** (A $g^{-1}$) | **C** (F $g^{-1}$) |
|---|---|
| 8.8 | 521 |
| 13.4 | 480 |
| 17.8 | 450 |
| 26.0 | 391 |
| 31.0 | 373 |

## List of Figures

**Figure 1**. A) Typical SEM top-view image, B and C) TEM and HRTEM images observed for $MnO_2$@IFMC nanocomposite

**Figure 2**. EDAX plot recorded for $MnO_2$@IFMC nanocomposite (Cu L and K lines are attributed to the underlying copper grid)

**Figure 3**. XRD plot recorded for $MnO_2$@IFMC nanocomposite

**Figure 4**. a) Nitrogen adsorption–desorption isotherms, and b) Typical BJH plot recorded for $MnO_2$@IFMC nanocomposite

**Figure 5**. TGA plots obtained for $MnO_2$@IFMC nanocomposite under air atmosphere.

**Figure 6**. Cyclic voltammograms recorded for $MnO_2$@IFMC nanocomposite electrode in a 1.0 M $Na_2SO_4$ solution.

**Figure 7**. Specific capacitances of $MnO_2$@IFMC nanocomposite electrode calculated from CV curves as a function of scan rate.

**Figure 8**. Galvanostatic charge-discharge curves of $MnO_2$@IFMC nanocomposite electrode at different current densities in a 1.0 M $Na_2SO_4$ solution (a) and the plot of specific capacitance estimated for $MnO_2$@IFMC electrode against current density (b)

**Figure 9**. Ragone Plot for $MnO_2$@IFMC nanocomposite electrode

**Figure 10**. Nyquist plot of $MnO_2$@IFMC nanocomposite electrode carried out at the open circuit potential

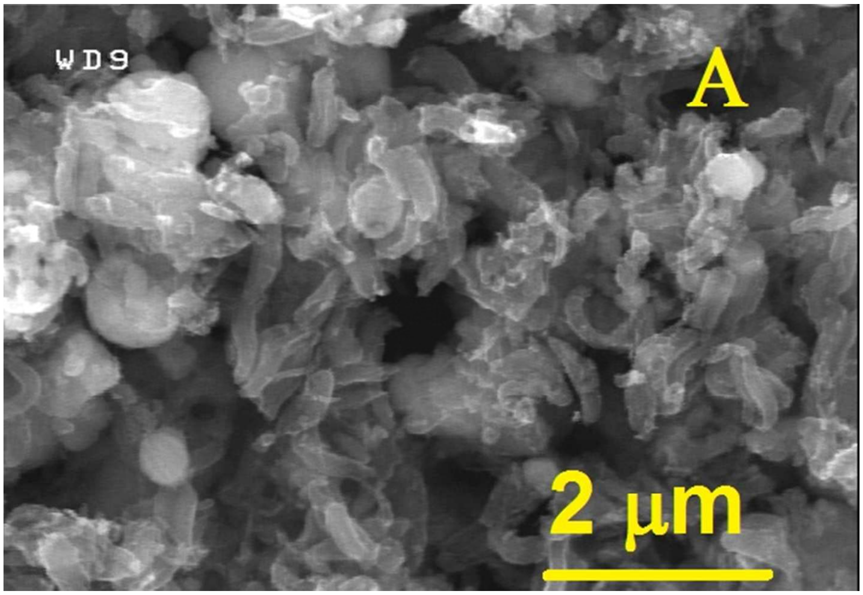
WD9
A
2 µm

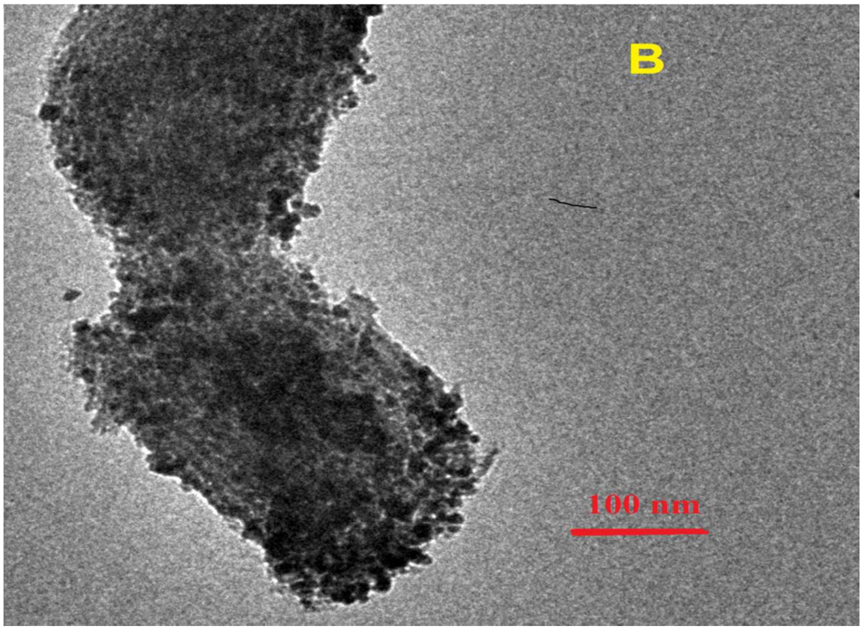
B
100 nm

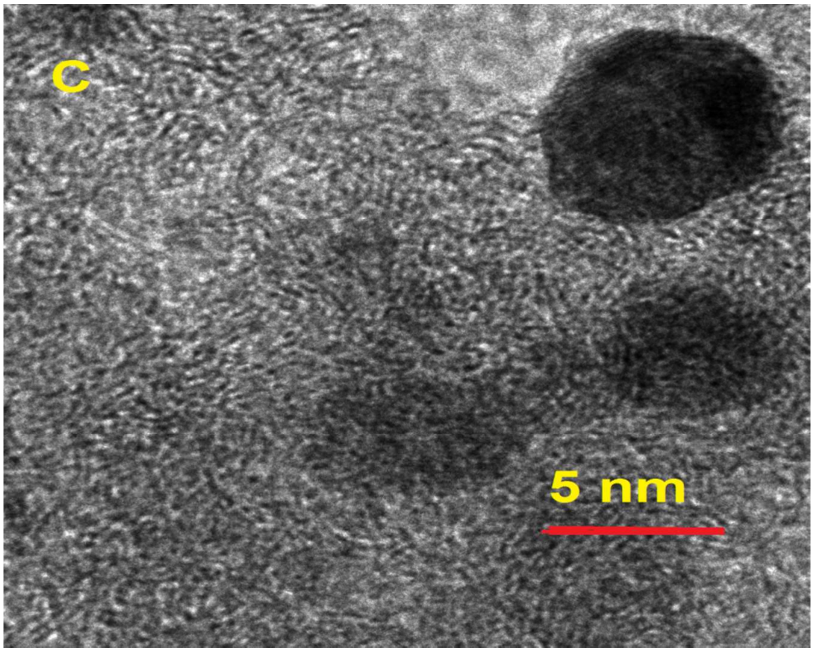

Figure 1

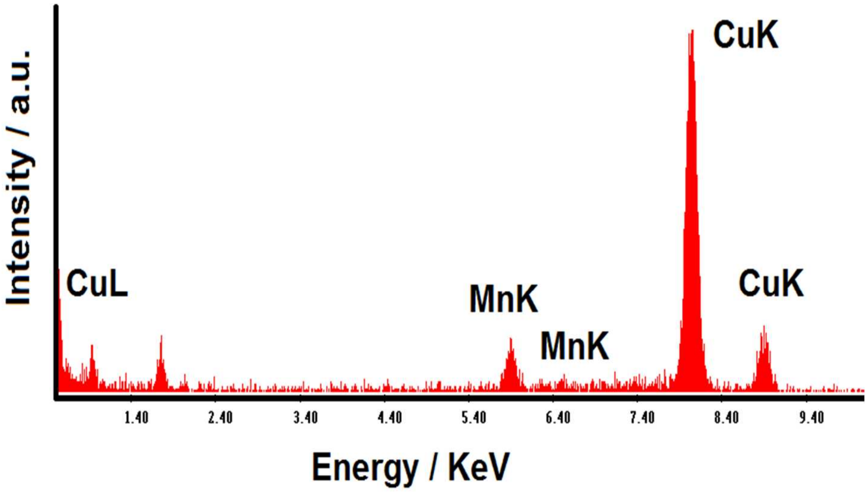
CuK
CuL
MnK
MnK
CuK
Intensity / a.u.
1.40
2.40
3.40
4.40
5.40
6.40
7.40
8.40
9.40
Energy / KeV

Figure 2

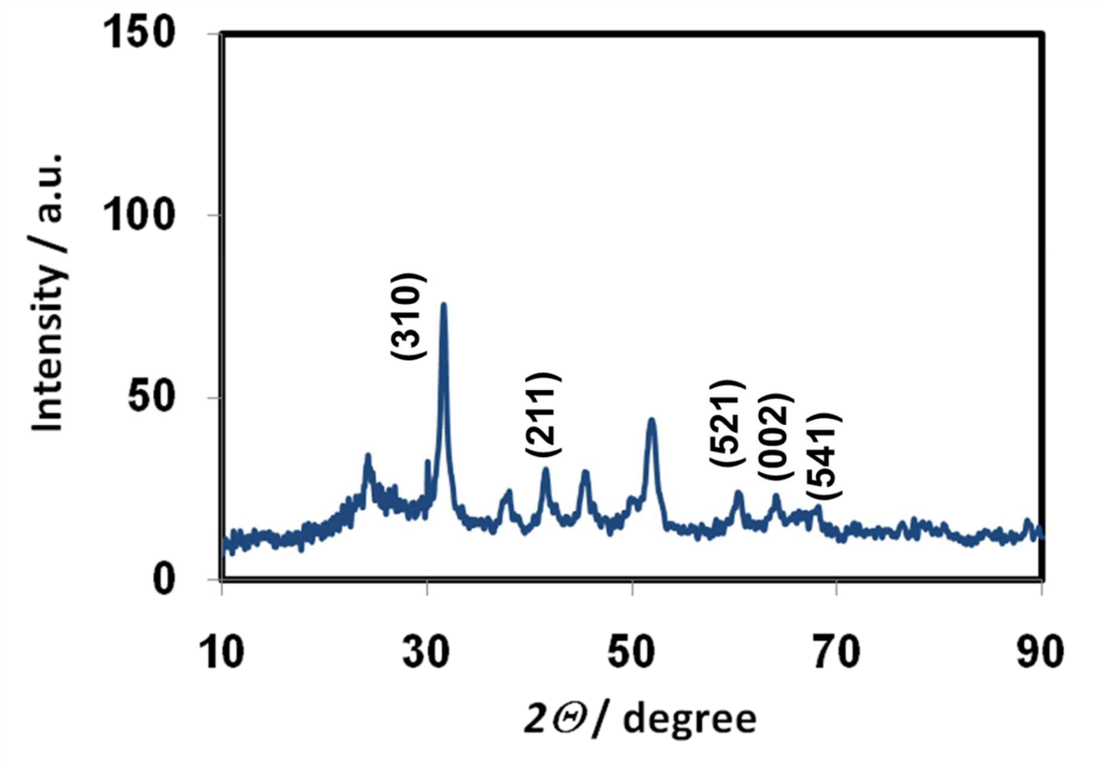
150
100
50
0
Intensity / a.u.
10
30
50
70
90
2Θ / degree
(310)
(211)
(521)
(002)
(541)

Figure 3

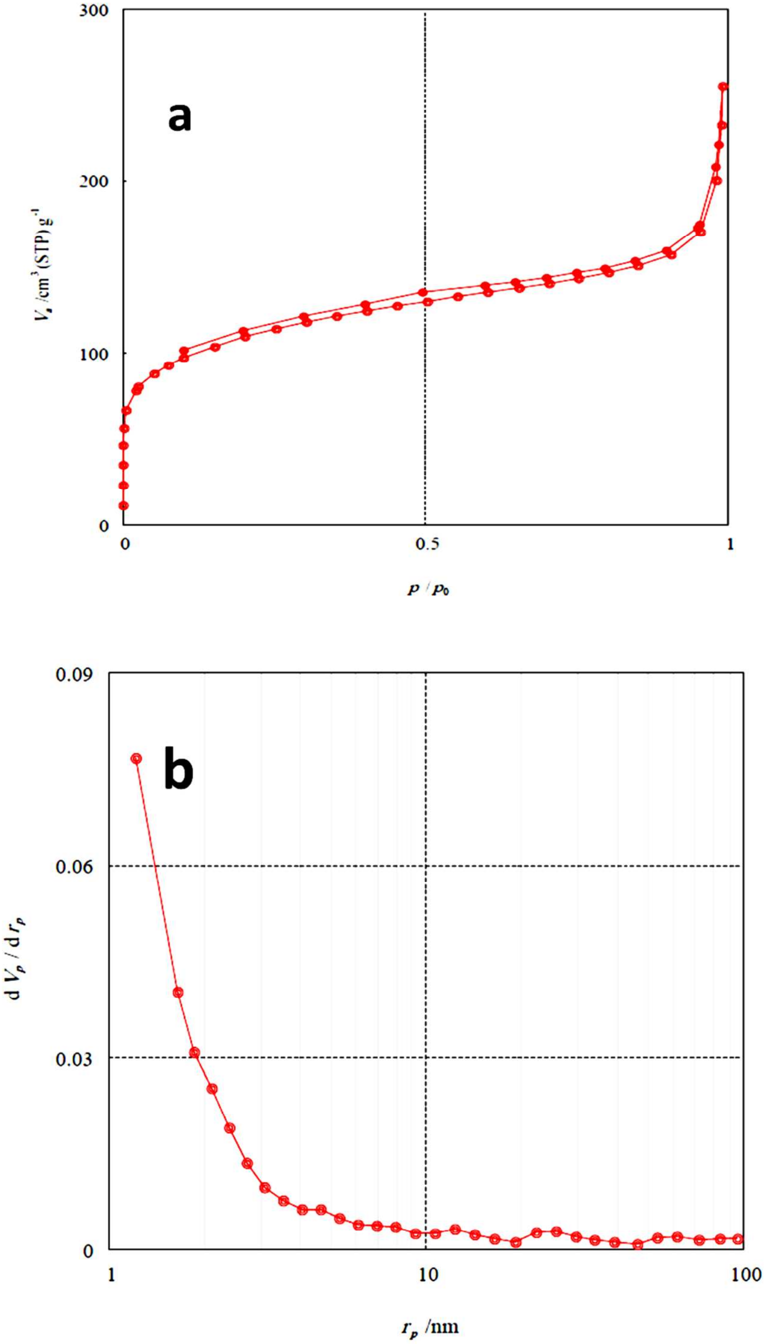
a
300
200
100
0
V_a /cm^3 (STP) g^-1
0
0.5
1
p / p0
b
0.09
0.06
0.03
0
d V_p / d r_p
1
10
100
r_p /nm

Figure 4

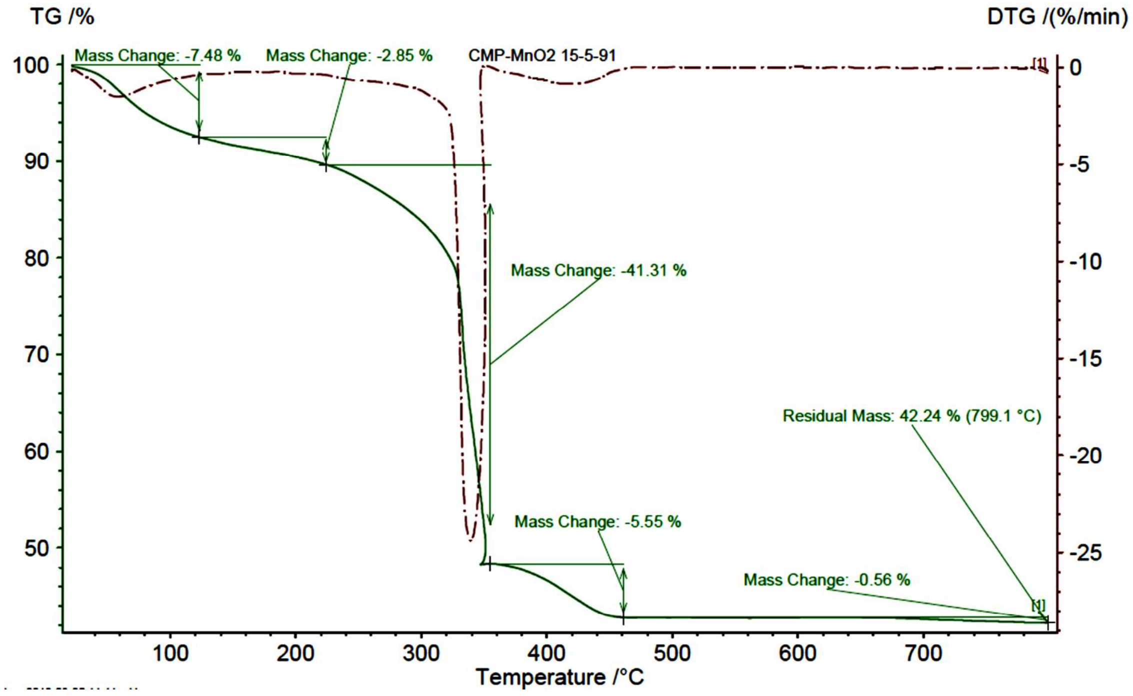
TG /%
DTG /(%/min)
Mass Change: -7.48 %
Mass Change: -2.85 %
CMP-MnO2 15-5-91
[1]
Mass Change: -41.31 %
Residual Mass: 42.24 % (799.1 °C)
Mass Change: -5.55 %
Mass Change: -0.56 %
[1]
100
90
80
70
60
50
0
-5
-10
-15
-20
-25
100
200
300
400
500
600
700
Temperature /°C

Figure 5

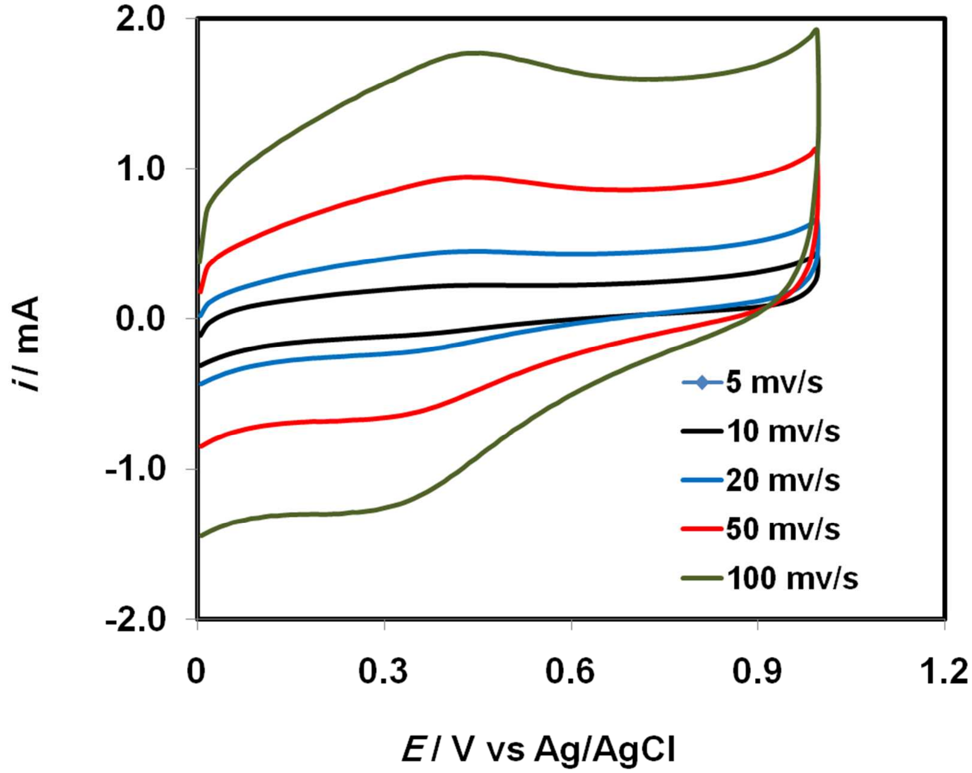
2.0
1.0
0.0
-1.0
-2.0
*i* / mA
0
0.3
0.6
0.9
1.2
*E* / V vs Ag/AgCl
5 mv/s
10 mv/s
20 mv/s
50 mv/s
100 mv/s

Figure 6

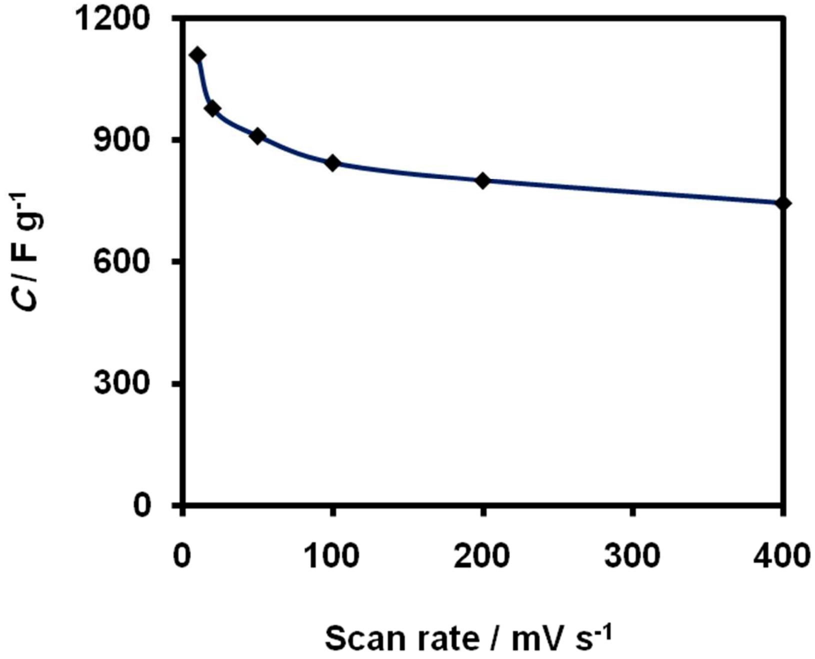

Figure 7

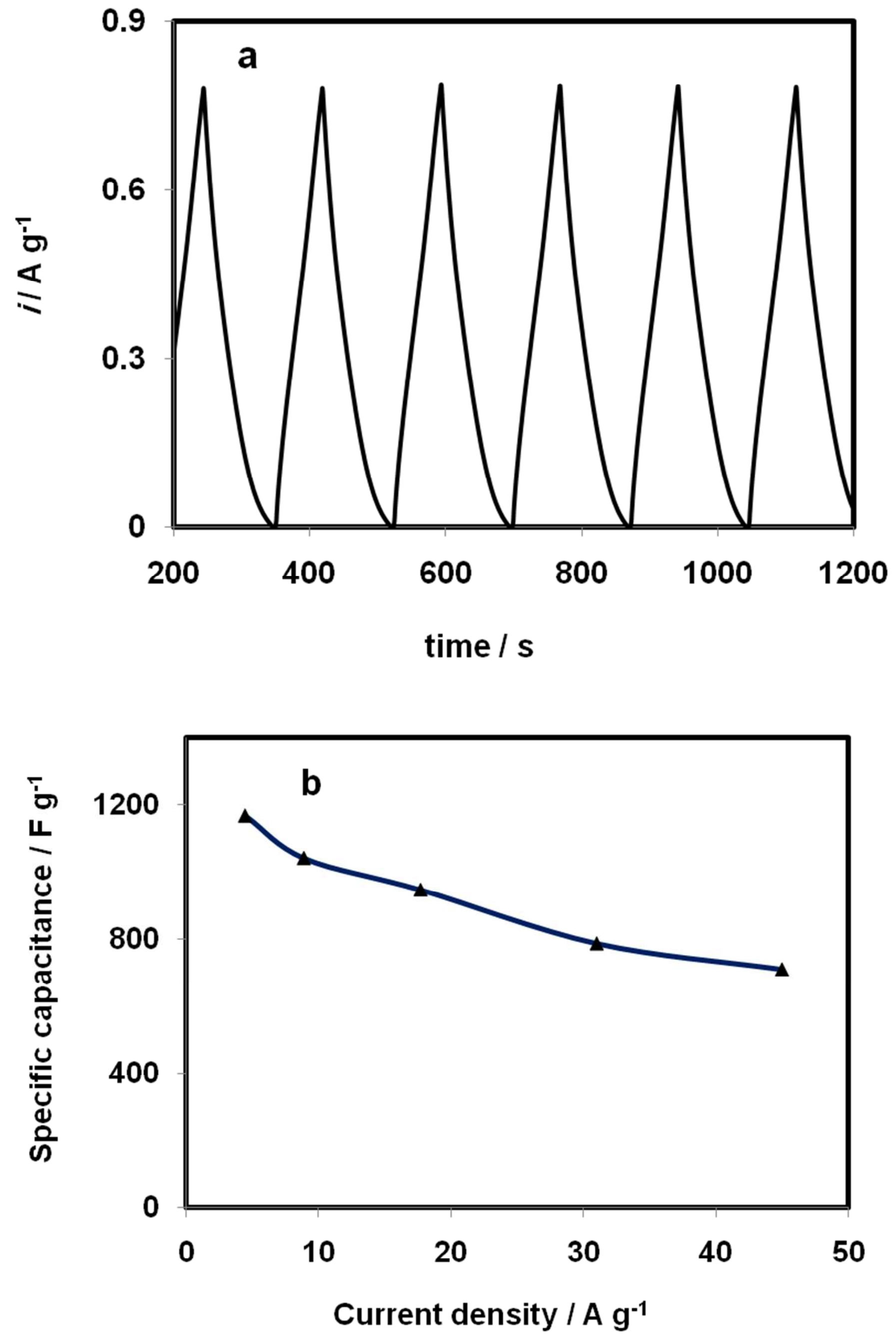
a
0.9
0.6
0.3
0
$i$ / A g$^{-1}$
200
400
600
800
1000
1200
time / s
b
1200
800
400
0
Specific capacitance / F g$^{-1}$
0
10
20
30
40
50
Current density / A g$^{-1}$

Figure 8

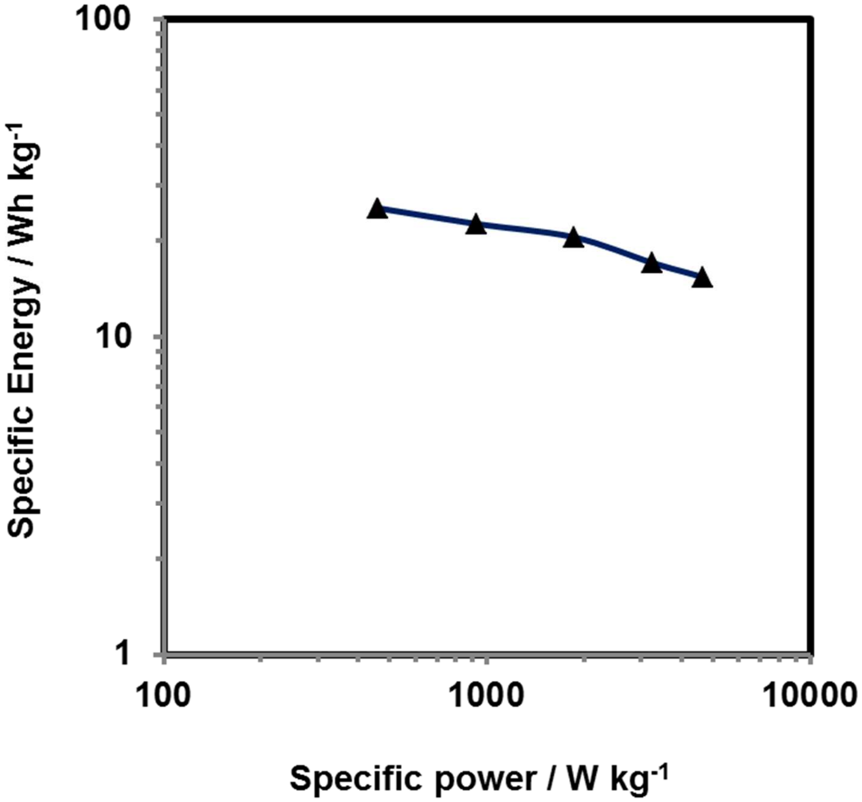
100
10
1
100
1000
10000
Specific Energy / Wh kg$^{-1}$
Specific power / W kg$^{-1}$

Figure 9

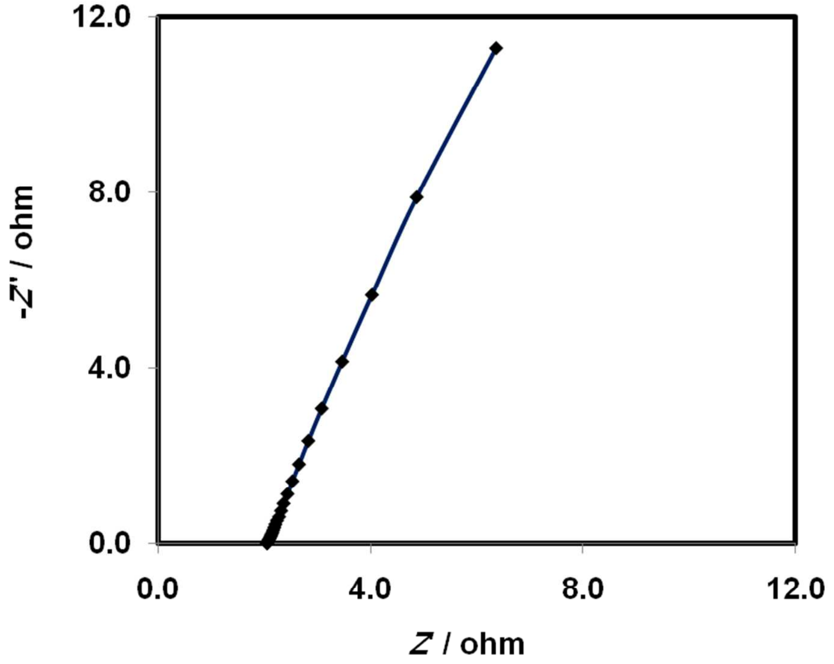

Figure 10